



OPEN

Taguchi optimisation of ZnO and GO-integrated HA nanocomposite with improved antibacterial performance

Hossein Mohammadi^{1,2}, Negin Bashardoust³, Michal Petrů⁴, Mona Ebadi⁵, Salmia Beddu², Mohsen Safaei^{6,7}✉ & Seyed Saeid Rahimian Koloor⁸✉

The concern associated with hydroxyapatite (HA) in dental applications is biofilm formation on the surface, causing tooth decay. Combining HA with antibacterial agents has great potential to avert biofilm formation and increase its antibacterial activity. The novelty of this study lies in the systematic optimization of HA/ZnO/GO nanocomposite synthesis using the Taguchi L9 orthogonal array method (3 factors: HA, GO, and ZnO). Unlike previous HA/GO/ZnO studies focused solely on compositional or biological evaluations, this approach identifies the optimal synthesis parameters statistically, attaining enhanced antibacterial performance. The structural arrangement of the nanocomposite was examined using XRD, TEM, and FESEM. Moreover, the successful interfacial interaction between HA, ZnO, and GO were verified in the nanocomposite through FTIR, TEM, and EDX analyses. The highest effective antibacterial activity was observed for the nanocomposite synthesised under experiment 3 (20.08 mg/mL HA, 0.03 mg/mL GO, and 4.88 mg/mL ZnO), in which the HA/ZnO/GO nanocomposite showed a significantly lower bacterial survival rate of $0.61 \log_{10}$ CFU/mL than that of $0.97 \log_{10}$ CFU/mL for pure HA. The results demonstrated the effective antibacterial properties of the nanocomposite, suggesting that the HA/ZnO/GO nanocomposite can be used in oral health applications.

Keywords Hydroxyapatite, Zinc oxide nanoparticles, Graphene oxide, Taguchi method, Antibacterial

Dental caries has become a serious health issue worldwide, which imposes a significant cost on the health economy¹. Once the tooth surface is exposed to bacteria for a long time, it is susceptible to dental caries due to the colonisation of supragingival plaque on its surface and the reduction of saliva flow²⁻⁴. The exopolysaccharides, particularly *mutans*-derived glucans, are the key matrix component in oral biofilm associated with dental caries⁵. This is because the dietary sucrose is metabolised into insoluble exopolysaccharides, which increase the bacterial adhesion and accumulation on the tooth surface, promoting the formation of acidogenic biofilm, causing caries⁶. Therefore, *S. mutans* has been considered the key modulator in the development of dental caries. To tackle this, suitable materials that are capable of reducing *S. mutans* biofilm survival are crucial.

Hydroxyapatite (HA) is a bioceramic with a comparable chemical composition to the mineralised phase of teeth⁷. It has gained prominence for dental applications⁸ such as an anti-caries agent in the treatment of dental lesions. A previous study demonstrated HA toothpaste as an anti-caries agent to restore demineralised enamel surface⁹. However, according to previous studies, pure HA has no bacterial reduction against bacterial strains or restricted antibacterial behaviour^{10,11}. The low antibacterial activity of HA in its pure phase might hinder its

¹School of Materials and Mineral Resources Engineering, Universiti Sains Malaysia, Engineering Campus, Nibong Tebal 14300, Penang, Malaysia. ²Department of Civil Engineering, College of Engineering, Institute of Energy Infrastructure (IEI), Universiti Tenaga Nasional, Jalan IKRAM-UNITEN, 43000 Kajang, Selangor, Malaysia. ³Students Research Committee, Kermanshah University of Medical Sciences, Kermanshah, Iran. ⁴Faculty of Mechanical Engineering, Technical University of Liberec, Studentska 2, Liberec 461 17, Czech Republic. ⁵Engineering Materials & Structures (eMast), ikohza, Malaysia-Japan International Institute of Technology (MJIIT), Universiti Teknologi Malaysia, 54100 Kuala Lumpur, Malaysia. ⁶Advanced Dental Science and Technology Research Centre, School of Dentistry, Kermanshah University of Medical Sciences, Kermanshah, Iran. ⁷Division of Dental Biomaterials, School of Dentistry, Kermanshah University of Medical Sciences, Kermanshah, Iran. ⁸Institute for Nanomaterials, Advanced Technologies and Innovation, Technical University of Liberec, Studentska 2, Liberec 461 17, Czech Republic. ✉email: safaei@kums.ac.ir; seyed.rahimian@tul.cz

usage in dentistry^{12,13}. This is due to the adhesion and colonisation of bacteria resulting from the absorption of organic substances on their surface, which seems to increase the possibility of bacterial inflammation¹⁴.

One way to circumvent this challenge is the loading of antibiotics such as gentamicin into HA. Nevertheless, the potential risk of increased antibiotic resistance compromises the efficiency of antibiotics. Therefore, the development of nanocomposites^{15,16} with antibacterial properties is in dire need to prevent implant-related infections. Nanotechnology has been explored to increase the antibacterial effects of HA^{13,14}. It involves the incorporation of nanoparticles or nanomaterials such as yttrium oxide (Y_2O_3)¹⁷, cadmium-selenite (CdSe)¹⁸, aluminium oxide (Al_2O_3)¹⁹, holmium oxide (Ho_2O_3)²⁰, copper oxide (CuO)²¹, cuprous oxide (Cu_2O)²² and ZnO^{11,19,23,28,29} into HA to overcome its limitations²³ due to their specific ability against bacteria^{23–25}. One of their features is the generation of reactive oxygen species (ROS) via oxidation from direct contact with bacteria²⁶. Among them, zinc oxide (ZnO), as a non-toxic, low-cost, and biocompatible material, has been used as a reinforcing phase in previous studies. For example, Rana et al. have shown that ZnO significantly enhanced the photodegradation activity of a floating photocatalyst against antibiotics as harmful pollutants due to the strong photocatalytic capabilities of ZnO²⁷. Also, Soni et al. modified ZnO with oxygen vacancies and found that the oxygen vacancy-rich ZnO improved the photocatalytic activities against harmful pollutants (antibiotics)²⁸. Batra et al. reviewed the green-synthesised ZnO nanoplateform as an environmental photocatalyst, which exhibits excellent non-toxicity and biocompatibility which making it a potential alternative candidate for conventional remediation strategies²⁹. Graphene oxide (GO) is a safe and biocompatible material with antibacterial activity that can be used as a reinforcing phase in HA^{30,31}. Thus, the primary objective of this study is to improve the properties of HA by adding GO and ZnO.

One of the powerful statistical tools for experiment design is the Taguchi method, which was proposed by the Japanese statistician Genichi Taguchi. This method helps to minimise performance variability by optimising design parameters that influence the quality of the final product³². Additionally, it allows further, simultaneous analysis of multiple factors with minimal numbers of trials, which reveal the contribution of individual factors and predict the optimum condition³². Previous studies have reported various HA/GO/ZnO ternary composites with promising antibacterial and biocompatible properties^{12,34–38}; however, these studies focused mainly on compositional or biological evaluations without statistical optimization of synthesis parameters. To the best of the author's knowledge, the optimization of HA/ZnO/GO nanocomposite synthesis was not reported in the literature. Therefore, the novelty of the present study is portrayed primarily in systemic optimization of HA/ZnO/GO nanocomposite using the Taguchi method with the highest antibacterial properties against *S. mutans*. In the present work, the Taguchi L9 orthogonal array (OA) is applied to identify and optimize the most influential factors governing the nanocomposite antibacterial performance. This statistically guided approach provides an efficient pathway to develop HA-based antibacterial nanocomposite with prospective dental applicability. To provide a clear visual overview of nanocomposite synthesis and characterisation in this study, Fig. 1 represents a schematic summarising the key preparation stages in the development of nanocomposite. This supports the conceptual framework of the study and guide the readers into detailed preparation and characterisation.

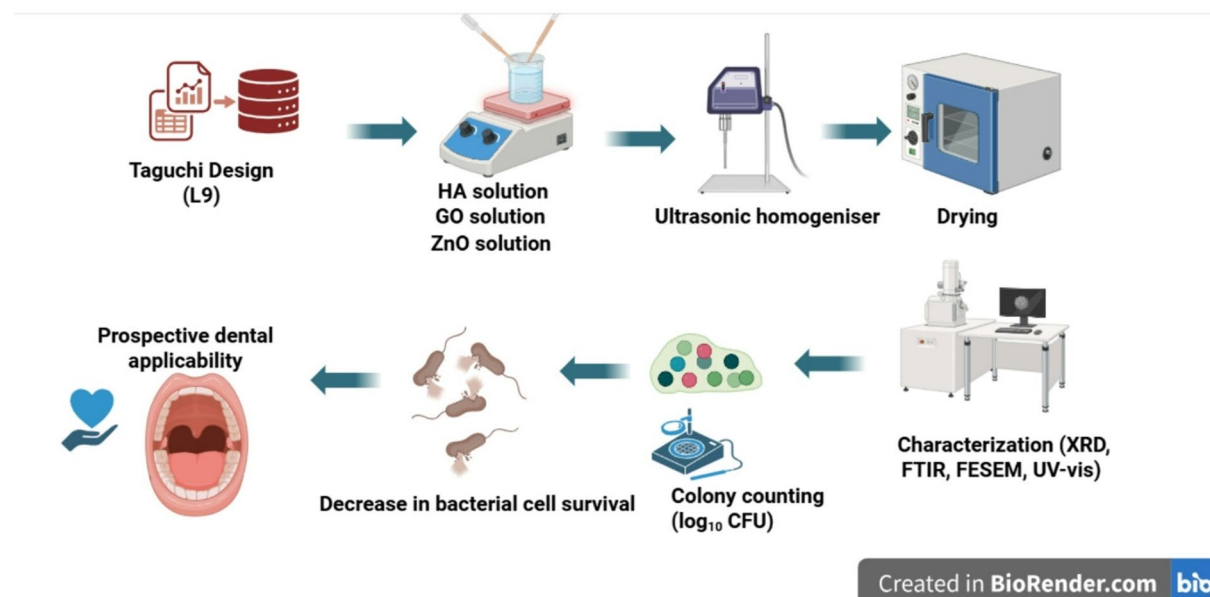


Fig. 1. Schematic illustration of the synthesis pathway study design and material preparation of the nanocomposite. The diagram summarizes the key steps involved in material preparation and highlights the sequential stages involved in synthesizing the HA/ZnO/GO nanocomposite and outlines its prospective biomedical and antimicrobial applications.

Materials and methods

Synthesis of ZnO nanoparticles

The Zn (CH_3CO_2)₂•2H₂O and NaOH were used to synthesise ZnO nanoparticles. In the first step, they were dissolved in deionised water to prepare 0.2 M NaOH and 0.1 M Zn (CH_3CO_2)₂•2H₂O solutions, respectively. Then, these solutions were evenly stirred at 750 rpm in the beaker for 2 h at 60 °C, forming a transparent milky solution. Then, the quick centrifugation of the solution at 4500 rpm for 2 min resulted in precipitates. Finally, the ZnO nanoparticles were prepared by rinsing precipitates with deionised water and acetone, followed by oven drying at 75 °C for 6 h³³.

Synthesis of HA nanoparticles

The calcium nitrate tetrahydrate (Ca(NO₃)₂•4 H₂O, 99%) and diammonium hydrogen phosphate ((NH₄)₂HPO₄, 98%) were purchased from Sigma-Aldrich (USA) and used as precursors for the hydroxyapatite (HA) synthesis. Graphene oxide (GO, 99.7%) and zinc oxide (ZnO, 99.7%), were obtained from Inframat Advanced Materials (USA). All chemicals were of analytical grade and used without further purification. Deionized water was used for all solution preparations and washing steps throughout the experiments. For HA synthesis, the calcium nitrate tetrahydrate and diammonium hydrogen phosphate were dissolved in deionized water to prepare the Ca-containing and P-containing solutions. After that, the solutions were diluted to 350 mL and 250 mL, respectively, using deionized water. In all experiments, pH of solution was adjusted between 9 ~ 10 using ammonia solution, and the final mixture was magnetically stirred at 400 rpm for 2 h at room temperature (25 °C) ensuring complete homogenization. Then, the centrifugation of solution at 3000 rpm (~ 1000×g) for 5 min resulted in precipitates. Finally, the HA nanoparticles were obtained by washing the precipitates three times with deionized water followed by drying in a vacuum oven at 80 °C for 12 h to ensure complete moisture removal without affecting the crystal structure³⁴.

Synthesis of HA/ZnO/GO nanocomposite

To prepare the nanocomposite samples, each of HA, ZnO, and GO were each magnetically stirred at 500 rpm for 1 h using distilled water as solvent to ensure complete dissolution. Then, the precursor solutions (HA, ZnO, GO) were each sonicated using a high-density ultrasonic homogenizer (total energy \approx 13.6 kJ at ambient temperature for 10 min at ambient temperature to obtain uniform suspension. In the next step, GO and ZnO suspensions were simultaneously added to the HA suspension dropwise. Finally, the resulting mixture was subsequently dried in a vacuum oven at 100 °C for 24 h to remove moisture without affecting the nanocomposite structural integrity. This process yielded the HA/ZnO/GO nanocomposite powders for further characterization and antibacterial testing. To determine the optimised synthesis conditions for HA/ZnO/GO nanocomposites, nine experiments including different ratios of nanoparticles were designed according to the Taguchi method by employing an orthogonal array (OA). The suspensions of nanoparticle components comprised 20.08 mg/mL, 40.16 mg/mL, and 80.32 mg/mL HA nanoparticles, 0.01 mg/mL, 0.02 mg/mL, and 0.03 mg/mL GO nanoparticles, and 2.44 mg/mL, 4.88 mg/mL, and 7.32 mg/mL ZnO were synthesised to prepare nine samples of nanocomposites. To prepare nanocomposite samples, the solutions of HA, GO, and ZnO were separately stirred on a magnetic stirrer for 1 h using distilled water as a solvent. Then, these three solutions were dispersed for 15 min using an ultrasonic homogeniser. In the next step, the suspensions containing ZnO and GO nanoparticles were added simultaneously to the HA suspension dropwise. Finally, the resulting suspension was oven-dried at 100 °C for 24 h, which resulted in nanocomposite precipitates³⁴.

Bactericidal properties

To evaluate the bactericidal activity of synthesised HA/ZnO/GO nanocomposites against the *S. mutans* (ATCC35668), the *S. mutans* strain was purchased from the Research Organisation for Science and Technology in Iran. The *S. mutans* biofilm was formed by the addition of bacterial suspension to a 96-well culture plate followed by incubation under aerobic conditions for 72 h at 37 °C. After the *S. mutans* biofilm was formed, the synthesised nanocomposites were added to each well-culture plate based on the 9 experiments designed by the Taguchi method, and the plates were incubated for 24 h. To calculate the number of living cells, the bacterial cells were rinsed with 1 mL PBS and were homogenised using a vortex after three times washing^{35,36}. To conduct the colony-forming unit (CFU), the bacterial suspension was diluted 10 times using serial dilution. After that, they were incubated on the culture plate containing brain heart infusion (BHI) extract for 24 h at 37 °C. After incubation, the mean values of colonies were obtained for 9 experiments. All the experiments were performed in triplicate^{35,36}. The antibacterial response data (\log_{10} CFU/mL) from experimental runs were analysed using Taguchi L9 (3³) orthogonal array design to determine the main effects of HA, ZnO, and GO concentrations. Each factor was varied independently at three levels: HA: 20.08, 40.16, 80.32 mg/mL; ZnO: 2.44, 4.88, 7.32 mg/mL; GO: 0.01, 0.02, 0.03 mg/mL. Mean responses for each factor level were computed from \log_{10} CFU/mL and variance was estimated from the residual sum of squares obtained from ANOVA. The residual degree of freedom (DOF) was used to estimate the error term and 95% confidence intervals (CI) were applied for clarity. All calculations were verified manually. Additionally, to determine the effects of HA, ZnO and GO contribution on the antibacterial activity, for each factor, the sum of square, variance, F-ratio, and pure sum were provided. The F-statistics was evaluated against the F-distribution (df1 and df2) at $\alpha = 0.05$. Factors with higher F-values and *p*-values lower 0.05 were considered a significantly different. ANOVA assumes that each population is normally distributed and errors are independent.

Characterisation

The X-ray diffraction (XRD) analysis is used to determine the phase purity and the size of the nanoparticles³⁷. The XRD diffraction patterns of individual components and the nanocomposite were attained using CuK α

radiation (Bruker D8, $\lambda = 1.542 \text{ \AA}$, 40 kV and 30 mA). The scans were performed from $20^\circ \leq 2\theta \leq 80^\circ$ with a step size of 0.02° and a dwell time of 1 s per step. Diffraction peaks were identified according to Joint Committee (JCPDS) reference card using PANalytical X'Pert Highscore Plus (see Fig. 1). Peak broadening arising from crystallite size and microstrain, was corrected for instrumental effects using a silicon standard³⁸. The corrected full width at half maximum (FWHM) values were used in the Scherrer equation (Eq. 1)³⁹ for the estimation of the average crystallite size, calculated from diffraction peaks (002), (221), (112), (300), and (130).

$$d = \frac{0.9\lambda}{\beta \cos \theta} \quad (1)$$

Where λ , β , and θ correspond to X-ray wavelength (1.54056 \AA), peak width at half maximum and peak position, respectively.

The Fourier transform infrared (FTIR) is performed to identify the functional groups in the synthesised nanoparticles³⁷. This provides information through the vibrational transition of molecular species resulting from their inherent excitation. The FTIR spectra of the nanocomposite were obtained under transmittance mode at 400–4000 cm^{-1} . Ultraviolet-visible (UV-Vis) spectroscopy is a technique that quantifies the light that is absorbed and scattered by a sample as a function of wavelength³⁷. The optical properties of individual components and nanocomposite were evaluated using UV-vis spectroscopy (Shimadzu, UV-160 A spectrometer) in the wavelength range of 200–800 nm. All spectra were baseline-corrected against deionized water as reference blank before analysis⁴⁰. Field-emission scanning electron microscopy (FESEM) is an extensively used technique to characterise nanostructures and nanomaterials⁴¹. It yields clear and less electrostatically distorted micrographs providing information on the shape, aggregation, and dispersion. Morphological features and elemental mapping of HA, ZnO, GO, and HA/ZnO/GO nanocomposite were observed by FESEM (TESCAN; MIRA3TESCAN operating at 15 kV) equipped with an EDX using a SAMX detector. For FESEM analysis, the samples were placed on a copper plate with a strip of double-sided conductive tape and they were further coated with gold by sputtering. Energy-dispersive X-ray spectroscopy (EDX) is an analytical technique that is used for chemical characterisation and elemental analysis of the samples³⁷. Transmission electron microscopy (TEM) is an important characterisation technique to obtain particle size distribution and morphology through direct imaging³⁷. The morphology of the HA/ZnO/GO nanocomposite was investigated by TEM (Philips EM208S at 200 kV). For TEM analysis, a small amount of sample was dispersed in ethanol under ultrasonication. Then, a drop of diluted sample was placed on the copper grid coated with a thin carbon film.

Results and discussion

XRD analysis

The crystallography and phase formation of nanoparticles and nanocomposite samples are presented in Fig. 2. For HA, all the characteristic peaks are recognizable and Miller's index of (211), (112), (222), and (213) in the angles of 31.95° , 31.12° , 46.87° , and 49.67° specified the HA phase (JCPDS 00-034-0010). The result indicates the formation of the single-phase HA with a hexagonal crystal structure, which agrees with the previous study reported in the literature⁴². The highest peak intensity was found in the plane (211). The XRD patterns of ZnO revealed Miller's index of (100), (002), (101), (102), (110), (103), (112), indicating that the major characteristic peaks are related to the ZnO phase (JCPDS 00-009-0432)⁴². The highest peak intensity was displayed on the plane (101). In the XRD pattern of GO NPs, the corresponding peak at the angle of 9.2° is related to Miller's index (001), verifying the presence of GO. A similar result was found in reference⁴³. In the XRD pattern of HA/GO/

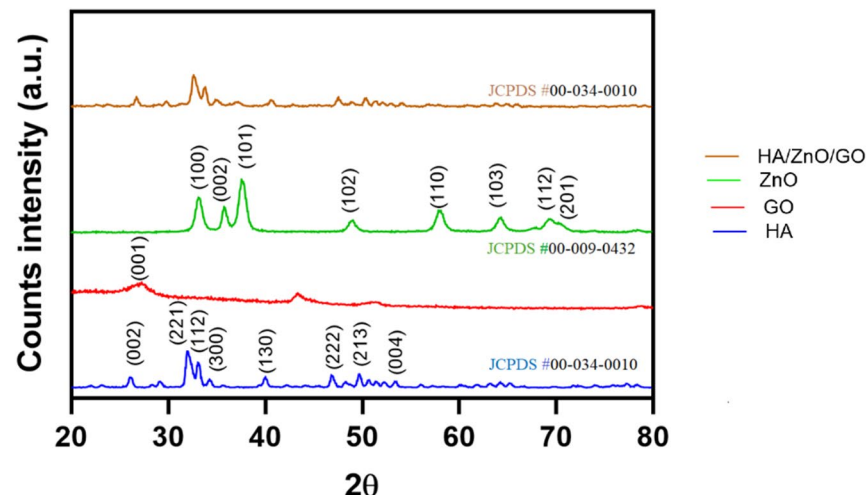


Fig. 2. XRD patterns of HA, GO, ZnO NPs and the HA/ZnO/GO nanocomposite.

ZnO, the characteristic peaks are associated with the structure of HA, matching the diffraction pattern (JCPDS 00-034-0010). This might be due to the low contents of GO and ZnO compared to HA as the bulk component.

This finding was supported by the previous reports⁴⁴. The characteristic peak related to GO vanished in the HA/ZnO/GO nanocomposite, indicating the interaction between the GO, HA, and ZnO. In addition, a decrease in XRD peak intensities at planes (100), (002), (102), and (110) was observed, which may be attributed to the peak broadening⁴⁵. The result of the crystallite size of HA and HA/GO/ZnO nanocomposite calculated from XRD data is shown in Table 1. As can be seen, the crystallite size of HA/GO/ZnO was 22.74 nm, which was lower than that of pure HA with a crystallite size of 28.12 nm.

FTIR analysis

Figure 3a shows the FTIR spectra of NPs components and the nanocomposite in the range of 400–4000 cm¹. As can be seen from FTIR spectra of HA, the peaks observed in the approximate area of 570 cm¹ and 1047 cm¹ are related to the bending and stretching vibration of the phosphate group (PO₄³⁻) in the crystal structure of HA. In addition, the weak peaks at 3414 cm⁻¹ and 632 cm⁻¹ are due to the stretching vibration of hydroxyl ions (OH⁻). According to Fig. 2, the absorbance peaks at 437 cm⁻¹ and 563 cm⁻¹ are associated with the stretching vibration of Zn–O⁴³. Furthermore, the peak at 3431 cm⁻¹ is ascribed to the stretching vibration of water molecules (O–H). The peak found at 1520 cm⁻¹ is related to the bending vibration of H–OH bonding⁴⁶. Figure 2 represents the FTIR spectra of GO. The absorption peak at 1099 cm⁻¹ is related to the stretching vibration of the carbonyl group (C–O). Furthermore, the peaks at 1629 cm⁻¹ and 1735 cm⁻¹ originated from stretching vibrations of the carbon–carbon group (C = C) and carboxyl group (C = O), respectively. The peak at 3426 cm⁻¹ was due to the bending and stretching vibration of OH groups absorbed on the GO. In the HA/ZnO/GO nanocomposite the intensity of bands was decreased. The spectrum, the PO₄³⁻ stretching band exhibited a slight leftward shift in wavenumbers from 1047 cm⁻¹ in pure HA to ~ 1035 cm⁻¹ and became sharp. However, the peak was broadened and less intense in the region of ~ 1047 cm⁻¹ for HA. This was likely due to the interactions between GO and HA (Fig. 3b). Our finding is consistent with previous study^{47,48}. The stretching band of C = O in 1735 cm⁻¹ shifted to lower wavenumbers at 1625 cm⁻¹ (Fig. 3c). This is caused by electrostatic interactions between C = O group in GO and OH group in HA. This finding is in good agreement with previous study⁴⁹. This subtle spectral changes suggest weak interfacial interactions among HA, ZnO, and GO components rather than new bond formation. The concurrent presence of Zn–O (563 cm⁻¹) and C–O (1099 cm⁻¹) absorption peaks verify the successful integration of ZnO and GO within the HA matrix. The results of the present study were further confirmed by the previous report⁵⁰.

UV-vis

Figure 4 depicts the UV spectra of the nanocomposite and its constituents, which were recorded in the wavelength range of 200–800 nm. The HA showed the absorbance peak at 208 nm, which is assigned to O²⁻→Ca²⁺ charge transfer⁵¹. For GO, an obvious sharp peak was observed at the wavelength of 240 nm, which agrees with the previous study⁵². This is the characteristic of the π–π* aromatic C = C bond⁵³. In addition, ZnO NPs peak at 363 nm in the wavelength range of 300–400 nm in the UV-vis region. Another report in the literature further confirmed this result⁵⁴. After the incorporation of GO and ZnO, the HA/GO/ZnO nanocomposite was shifted towards a higher wavelength and exhibited absorbance at 370 nm. This indicates a change in the energy bandgap and successful impregnation of GO and ZnO into the HA matrix⁵⁵.

Morphological evaluations

FESEM analysis

The morphologies of HA, GO, ZnO, and HA/GO/ZnO nanocomposite are shown in Fig. 5. As observed, pure HA shows a spherical morphology which has been agglomerated in some places. (Fig. 5a). The GO exhibited a typical layer structure (Fig. 5b)⁵⁶.

As can be seen in Fig. 4c, the ZnO showed spherical cotton-like morphology. This was in agreement with the previous report¹². Figure 4d shows the morphology of the HA/ZnO/GO nanocomposite. The results indicated that the addition of ZnO and GO affected the morphology of HA. This is ascribed to the inclusion of ZnO and GO in the HA structure. These findings were in good agreement with previous studies in the literature^{43,57}.

EDX analysis

The EDX analysis is routinely utilised for the investigation of spatially resolved elemental composition. The ratio of the bulk chemical composition is denoted by the atomic ratio in EDX. Figure 6 shows the EDX spectra of HA, GO, ZnO and the HA/ZnO/GO nanocomposite. From Fig. 6, it is evident that pure HA is comprised of calcium (Ca), phosphorus (P), and oxygen (O) (Fig. 5a). The elemental analysis of HA revealed 32.10 wt%, 15.21 wt%, and 46.17 wt% for Ca, P, and O, respectively.

Components	Average crystallite size (nm)
HA	28.12
ZnO	23.60
GO	5.68
HA/ZnO/GO	22.74

Table 1. Structural parameters of HA, GO, ZnO, and HA/ZnO/GO obtained from XRD data.

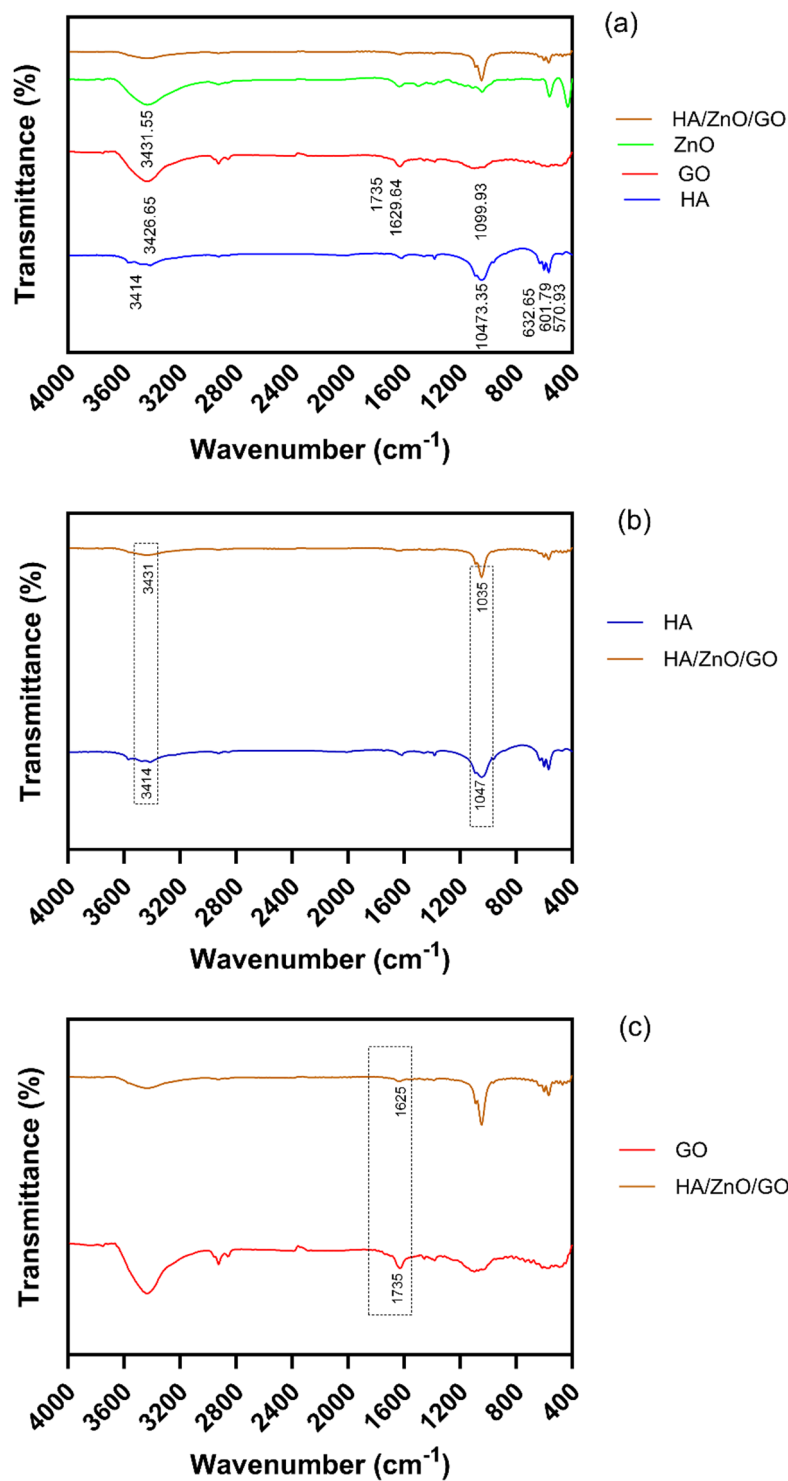


Fig. 3. FTIR spectra of (a) HA, GO, ZnO and HA/ZnO/GO nanocomposite, (b) comparison between spectra of HA and HA/ZnO/GO, and (c) comparison between spectra of HA and GO, respectively.

The highest weight% in HA was related to the O element (Fig. 6a). The EDX spectra of GO in Fig. 6b confirmed the presence of carbon (C) and oxygen (O) elements with 61 wt% and 37.32 wt%, respectively, in which the highest peak intensity was associated with the C element. Figure 6c shows the presence of zinc (Zn) and oxygen (O), with the highest peak intensity for the Zn element. The EDX spectra of ZnO revealed 76.62 wt% and 23.38 wt% for zinc (Zn) and oxygen (O) elements, respectively. The EDX spectrum of nanoparticles assured their purity.

The EDX spectrum of HA/ZnO/GO nanocomposite is shown in Fig. 6d, and the elemental composition is shown in Table 2. As can be seen, the EDX spectra confirmed the Ca, O, C, Zn and P with 20.70 wt%, 37.85

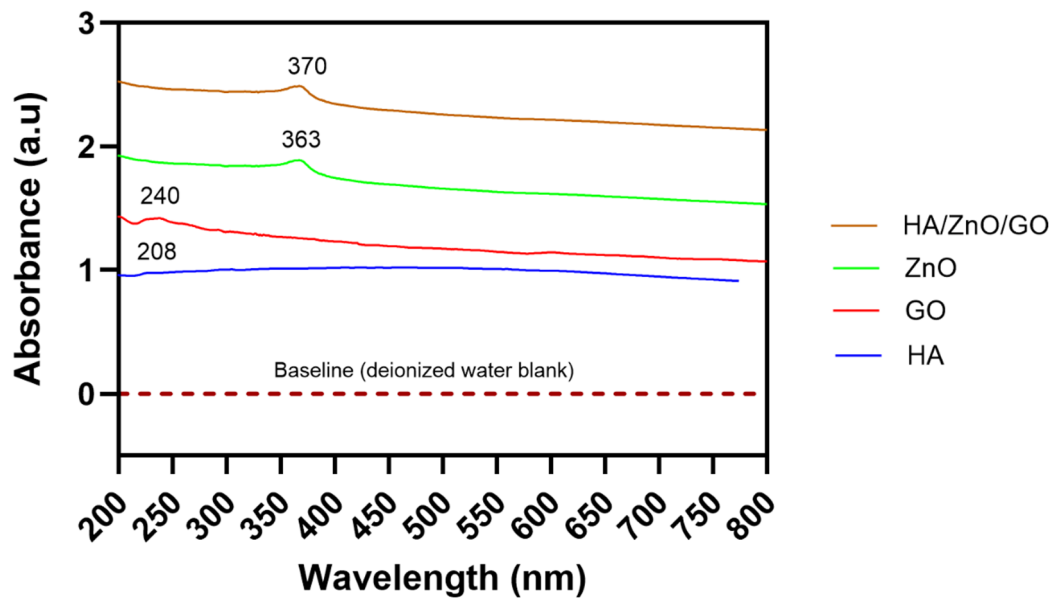


Fig. 4. UV-vis spectra of HA, GO, ZnO, and HA/ZnO/GO nanocomposite after baseline correction using deionized water as reference. The dashed horizontal line at Abs = 0 indicates the corrected baseline.

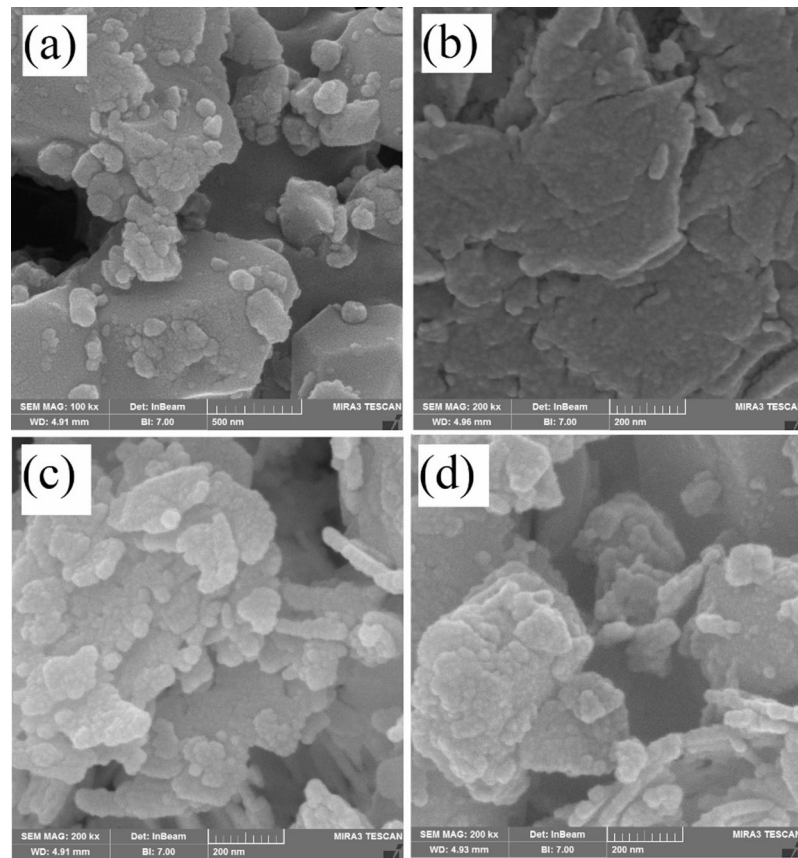


Fig. 5. FESEM micrographs of (a) HA, (b) GO, (c) ZnO, and (d) HA/ZnO/GO nanocomposites.

wt%, 13.02 wt%, 7.30 wt%, and 12.77 wt%, respectively. The highest peak intensity was associated with the Ca element in the spectra of the nanocomposite. GO is non-stoichiometric with an O: C ratio between 0.3 and 0.5, depending on the oxidation condition during synthesis⁵⁸. The C/O ratio in the present study was found to be 0.34, which proves the presence of GO. The Ca/P was approximately calculated as 1.66, slightly lower than that

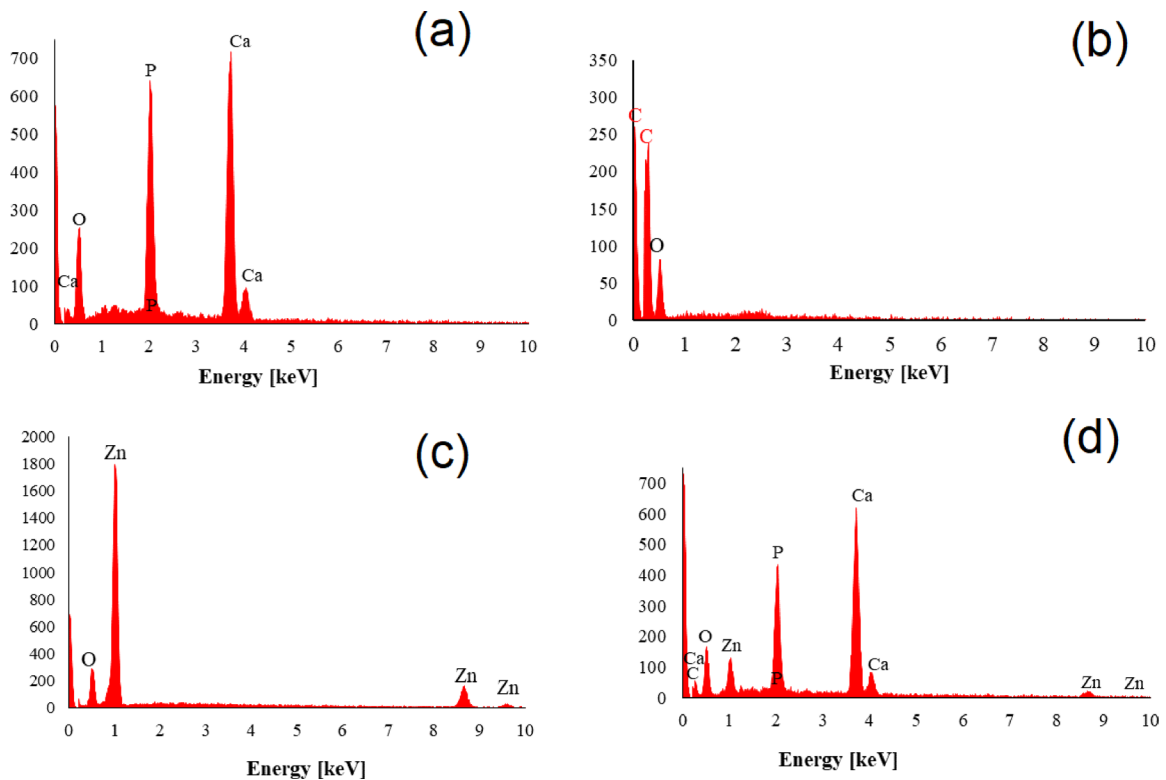


Fig. 6. EDX analysis of (a) HA, (b) GO, (c) ZnO, and (d) HA/ZnO/GO nanocomposite.

Element	Weight (%)
Ca K	20.70
P K	12.77
O K	37.85
C K	13.02
Zn K	7.30

Table 2. Elemental composition values obtained from HA/ZnO/GO nanocomposite.

of 1.67 for stoichiometric HA⁵⁹, confirming the presence of HA. Furthermore, the Ca/P ratio of HA/GO/ZnO was close to that of enamel and dentine, with a Ca/P ratio of 1.62 and 1.64, respectively⁶⁰. Mimicking the Ca/P ratio of dentine and enamel reveals this nanocomposite's better biocompatibility and bioactivity for prospective dental applications.

Mapping analysis

A FESEM micrograph of HA/ZnO/GO nanocomposite and its corresponding EDX mapping is shown in Fig. 7. It shows the elemental distribution maps and confirms the presence of elements including Ca, P, O, Zn, and C that compose HA/ZnO/GO nanocomposite.

TEM micrography

The TEM micrograph of the synthesised HA/ZnO/GO nanocomposite is shown in Fig. 8. It reveals an interconnected morphology in which the three components are uniformly distributed and in close physical contact, indicating good interfacial association among the components. This finding was supported by other reports in the literature. For example, Albalwi et al. have fabricated HA/Y₂O₃/GO ternary nanocomposite and found an integrated structure¹⁷. It was also observed that HA and ZnO nanoparticles were embedded within GO sheets. Ahmed et al. have fabricated HA/Co₃O₄/GO ternary nanocomposite and demonstrated the embedment of HA and Co₃O₄ into GO⁶¹. Taken together, the successful interfacial interaction between HA, ZnO, and GO were verified in the nanocomposite through FTIR, TEM, and EDX analyses.

Antibacterial analysis

The infection is known to impact the healing process negatively; therefore, the development of dental and bone biomaterials with antibacterial activity is desired³¹. In vitro tests, such as Agar, are commonly utilised for the

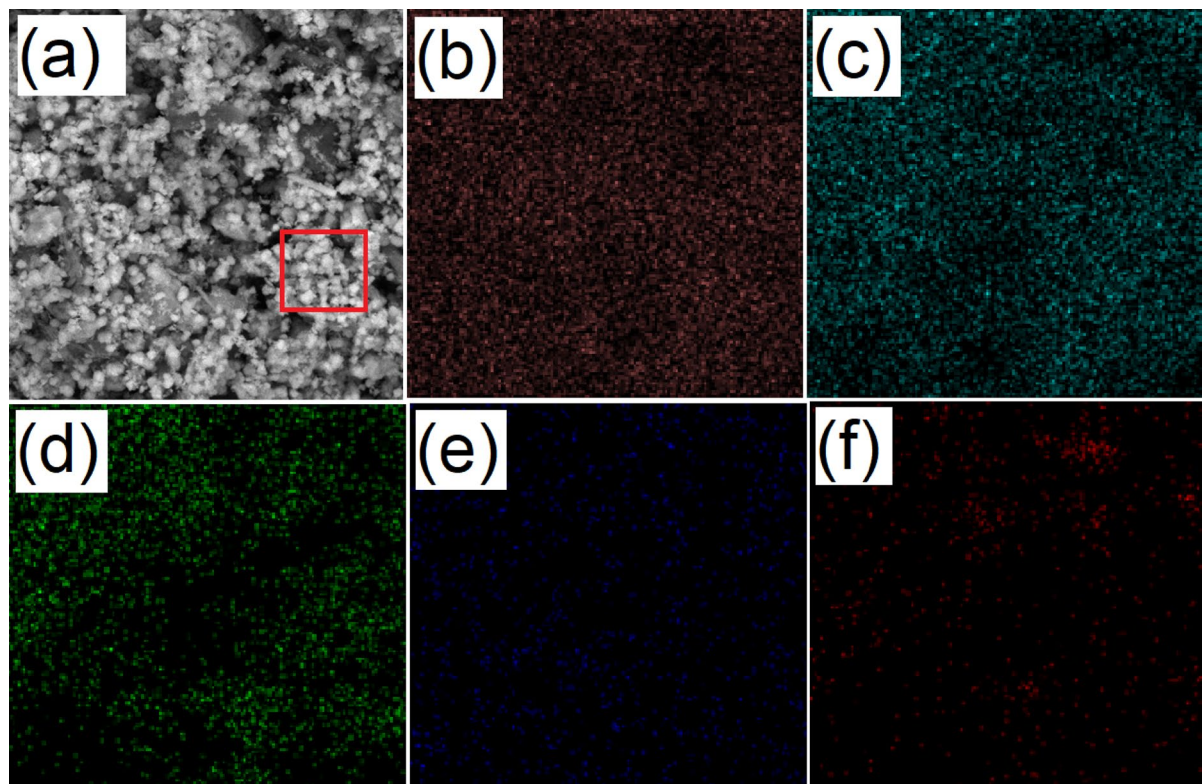


Fig. 7. Dispersion map of composition components on the surface of HA/ZnO/GO nanocomposite **(a)** FESEM micrograph, **(b)** Ca, **(c)** P, **(d)** O, **(e)** Zn, and **(f)** C, respectively.

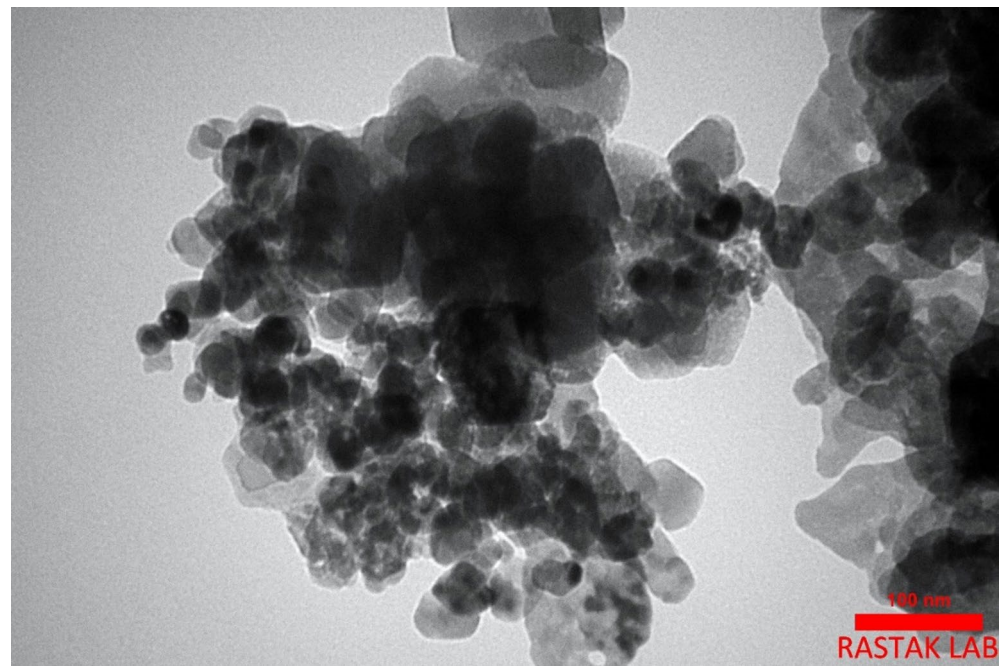


Fig. 8. TEM micrographs of HA/ZnO/GO nanocomposite.

assessment of antibacterial properties of biocomposite⁶². Cell counting is one of the techniques that employs the culturing of bacteria on Agar plates. The results of this method are reported in colony-forming units per millilitre (\log_{10} CFU/mL)⁶³. Table 3 shows the level of antibacterial activity of HA/ZnO/GO nanocomposite against *S. mutans* based on the Taguchi method. The results indicated that the synthesised nanocomposite under

Experiment	HA (mg/mL)			GO (mg/mL)			ZnO (mg/mL)			Bacterial survival (\log_{10} CFU/mL)
	20.08	40.16	80.32	0.01	0.02	0.03	2.44	4.88	7.32	
1		20.08			0.01			2.44		1.05
2		20.08			0.02			4.88		0.78
3		20.08			0.03			7.32		0.61
4		40.16			0.01			4.88		1.27
5		40.16			0.02			7.32		0.94
6		40.16			0.03			2.44		1.12
7		80.32			0.01			7.32		1.44
8		80.32			0.02			2.44		1.63
9		80.32			0.03			4.88		0.89

Table 3. Taguchi's design of experiments and effects of HA/ZnO/GO synthesised nanocomposites on the survival rate of *S. mutans*.

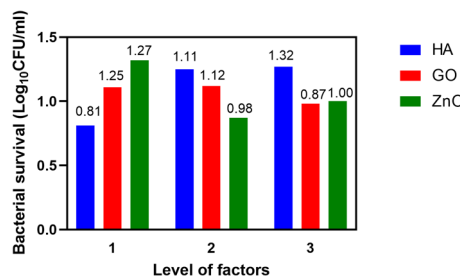


Fig. 9. The effect of HA, GO, and ZnO factors on the survival rate of *S. mutans*, separately.

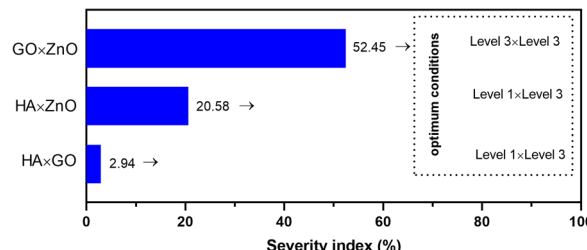


Fig. 10. The interactions of studied factors on the growth prevention of *S. mutans* biofilm.

experiment 3 (20.08 mg/mL HA, 0.03 mg/mL GO, and 7.32 mg/mL ZnO) possessed the strongest antibacterial activity against *S. mutans* and the lowest bacterial survival rate of 0.61 \log_{10} CFU/mL was found in the presence of the nanocomposite.

Figure 9 illustrates the variation in mean bacterial count (\log_{10} CFU/mL) at each factor level, with 95% confidence intervals (± 0.083) derived from residual variance. The narrow error indicates a good repeatability across the triplicate runs. Among factors, HA showed a progressive increase in bacterial count with concentration, proposing that excessive HA loading may decrease the antibacterial efficiency of the nanocomposite. Conversely, GO showed a clear decrease in \log_{10} CFU/mL with increasing concentration, confirming its strong antibacterial role, which is probably attributed to its sharp-edged morphology disrupting bacterial membrane. For ZnO, the minimum \log_{10} CFU/mL value was found at the intermediate concentration (4.88 mg/mL), implying an optimal loading beyond which the antibacterial activity may be reduced. Overall, the optimal synthesis condition from experiment 3 corresponds to HA = 20.08 (level 1), GO = 0.03 mg/mL (level 3), and ZnO = 4.88 mg/mL (level 2), maximises the antibacterial performance by interaction effects of three components in the nanocomposite (see Fig. 8).

The interaction effect of the factors on the survival rate of *S. mutans* is reported in Fig. 10. As can be observed, the third levels of GO and ZnO exhibited an interaction effect of 52.45%, the highest interaction effect on reducing bacterial growth. On the other hand, the HA in the first level and ZnO in the third level revealed an interaction effect of 20.58%. The lowest interaction intensity (2.94%) belonged to the first level of HA and the third level of GO. The results indicated that the concentrations of NPs impacted the antibacterial performance of the resultant nanocomposite⁶⁴.

Factor	F	p-value	95% CI (\pm)	Contribution (%)	Interpretation
HA	5.49	0.0126	± 0.083	37.98	Significant
GO	3.14	0.0652	± 0.083	18.09	Borderline
ZnO	2.19	0.1380	± 0.083	10.10	Not significant

Table 4. ANOVA summary for the antibacterial response (\log_{10} CFU/mL) of HA/ZnO/GO nanocomposites based on Taguchi L9(3^3) orthogonal array. p -values were computed using the F-distribution ($df_1=2$, $df_2=20$). The 95% confidence interval (± 0.083) was derived from the error variance and student's $t_{0.025,20}$ (2.086). Factors with $p < 0.05$ are statistically significant at the 95% confidence level.

Factors	Level	Contribution
HA	1	-0.27
GO	3	-0.21
ZnO	2	-0.10
Total contribution from all factors		-0.58

Current grand average of performance		1.08

Bacterial survival at optimum conditions		0.50

Table 5. The optimal synthesis of HA/ZnO/GO nanocomposites with the highest antibacterial activity.

The percentage of contribution of individual control factors could be determined by the analysis of variance (ANOVA)⁶⁵. Thus, it was used to postulate the percentage of contributions of three factors. The ANOVA of factors which affect the survival rate of *S. mutans* is tabulated in Table 4. The effectiveness of 37.98%, 18.09%, and 10.10% was found for HA, GO, and ZnO, respectively. The data suggested that the highest effect belonged to HA with an effectiveness of 37.98%. Moreover, the lowest effect belonged to ZnO with an effectiveness of 10.10%. The ANOVA results and percentage contribution demonstrated that HA significantly affected the antibacterial performance, contributing 37.98% of the total variation with F-ratio: 5.49 and p -value of 0.0126 (p -value < 0.05). This shows that HA concentration cause statistically significant changes in bacterial survival. GO contributed 18.09% of the total variation with F:3.14 and p -value of 0.0652 suggesting a borderline significant effect. Although the p -value was slightly higher than 0.05, this trend implies that GO levels have moderate influence on antibacterial efficiency. ZnO accounted for 10.10% of total variation with F:2.19 and a p -value of 0.1380 (p -value > 0.05). This suggests that ZnO concentrations may have minor effect on antibacterial performance. Taken together, the statistical ranking of factors HA > GO > ZnO follows the same trend with experimental findings verifying that HA concentration is the dominant factor in optimising the antibacterial performance, followed by GO as supporting factor, while ZnO provides supplementary contribution (Table 4). The 95% CI (± 0.083) for the mean \log_{10} CFU/mL indicated high precision measurement and low experimental variability across replicates. This narrow interval supports the reliability of the response data and confirms that the observed differences among factor levels are statistically meaningful rather than arising from random error.

The Taguchi design predicted the optimal synthesis conditions of HA/ZnO/GO nanocomposite with the highest bactericidal performance as illustrated in Table 5. The HA (level 1), the third GO (level 3) and the ZnO (level 2) causes a reduction in bacterial growth to 0.5 \log_{10} CFU/mL. This value predicted by Taguchi was close to the value obtained in experiment 3 (0.5 \log_{10} CFU/mL).

The possible explanation for strong antibacterial activity of HA/ZnO/GO nanocomposite against *S. mutans* can be attributed to combined contribution of GO and ZnO into HA structure. It was reported that GO exerts its bactericidal activity through physical and chemical mechanisms, which are associated with oxygen groups on its surface. As for the physical mechanism, the oxygen groups are directly attached to bacterial cell walls and the bactericidal activity is exerted. Furthermore, GO can cause direct damage to the structure of the bacteria by the sharp edges of its nanosheets³¹. On the other hand, the chemical mechanism forms ROS, which causes bacterial cell death⁶⁶. The ZnO exerts antibacterial properties through forming ROS species, damaging the bacterial membrane and releasing Zn^{2+} ions, which imbalances the charges of the bacterial cell walls, causing pathogen death. Although the findings of this study demonstrated enhanced antibacterial activity of HA through incorporation of ZnO and GO (nanocomposite), the detailed mechanistic validation is beyond its scope i.e. primary optimization. In reviewing recent literature on combination therapeutics, it is obvious that rigorous demonstration of "synergy" increasingly depends on quantitative statistical modeling, biological replicates, and appropriate control groups. For instance, in a study conducted by Acharya⁶⁷ applied the Bliss independence model across multiple concentration combinations to quantify synergistic effects beyond single-agent responses.

Likewise, Okechukwu et al. validated its enhanced efficacy through matched dosing controls and integrated in vitro and in vivo analyses, to strengthen the translational credibility of its findings⁶⁸. By comparing to our study, the enhanced antibacterial performance observed in our optimized HA/ZnO/GO nanocomposite is associated with combined contribution of GO, ZnO rather than mechanistic evidence. Nonetheless, this is qualitative and not yet supported by formal synergy modeling. Future investigations should include formal synergy evaluation (e.g., Bliss or Loewe models), and comprehensive biological controls, including cytocompatibility assays using dental-relevant cells to substantiate the mechanistic and translational potential of these nanocomposites as antibacterial dental biomaterials. In the present study, pure HA was used as the control for comparison with HA/ZnO/GO nanocomposite. However, future studies should incorporate other systematic control experiments using GO-, and ZnO-only samples, together with a positive antibacterial standard such as chlorhexidine. This can differentiate and give a better understanding of individual and combined effects. Furthermore, reactive oxygen species (ROS) quantification (e.g. DCFH-DA) and membrane integrity analyses through live/dead bacterial staining should be carried out to elucidate the underlying mechanisms of antibacterial activity. For prospective dental applicability of HA/ZnO/GO, the cytocompatibility evaluation remains as the essential next step prior to confirming its suitability for prospective dental applications. The present study preliminary focused on compositional optimization and antibacterial assessment; hence, in vitro cytocompatibility and biocompatibility analyses such as Almar Blue assays, live/dead staining using human dental pulp cells or human gingival fibroblast cells were not included within the scope of the current study. Future studies should incorporate these assays to evaluate the cellular and biological response associated with HA/ZnO/GO nanocomposite.

Conclusion

In the present study, HA/GO/ZnO nanocomposite was successfully synthesised for prospective dental application. The structural analysis corroborated the effective incorporation and interaction of GO and ZnO within HA, while structural and morphological evaluations (XRD, FTIR, TEM, FESEM) revealed an intimate interaction among the three constituents. Utilising the Taguchi design, the optimal synthesis conditions were identified (20.08 mg/mL HA, 0.03 mg/mL GO, and 4.88 mg/mL ZnO), which led to the highest antibacterial performance with a meaningfully reduced *S. mutans* survival rate of 0.61 CFU/mL. These findings highlight that the interaction effects of GO and ZnO noticeably disrupt the bacterial growth and biofilm formation in HA, overcoming the restrictions of pure HA (pure HA with no effective or low antibacterial performance). Overall, this study highlights the potential of HA/ZnO/GO nanocomposites as the next generation of dental biomaterials. Beyond antibacterial properties, future studies are warranted to investigate the mechanical properties, as well as in vitro and in vivo cellular studies to fully validate the clinical application of HA/GO/ZnO for oral health applications.

Data availability

All processed data supporting the findings of the present study inclusive of XRD, FTIR, UV-Vis, FESEM, TEM, EDX, and antibacterial assay results are presented within the manuscript. The original raw instrument files are no longer available due to storage constraints, however, all derived data necessary to reproduce the analyses are fully included in the manuscript.

Received: 12 August 2025; Accepted: 2 December 2025

Published online: 27 January 2026

References

1. Sampaio, A. A. et al. *Candida albicans* increases dentine demineralization provoked by *Streptococcus mutans* biofilm. *Caries Res.* **53**, 322–331. <https://doi.org/10.1159/000494033> (2019).
2. Simon-Soro, A., Guillen-Navarro, M. & Mira, A. Metatranscriptomics reveals overall active bacterial composition in caries lesions. *J. Oral Microbiol.* **6**, 25443. <https://doi.org/10.3402/jom.v6.25443> (2014).
3. Lenander-Lumikari, M. & Loimaranta, V. Saliva and dental caries. *Adv. Dent. Res.* **14**, 40–47. <https://doi.org/10.1177/0895937400140010601> (2000).
4. Chen, X. et al. Microbial etiology and prevention of dental caries: exploiting natural products to inhibit cariogenic biofilms. *Pathogens* **9**, 569 (2020).
5. Xiao, J. et al. The exopolysaccharide matrix modulates the interaction between 3D architecture and virulence of a mixed-species oral biofilm. *PLoS Pathog.* **8**, e1002623. <https://doi.org/10.1371/journal.ppat.1002623> (2012).
6. Klein, M. I., Hwang, G., Santos, P. H., Campanella, O. H. & Koo, H. *Streptococcus mutans*-derived extracellular matrix in cariogenic oral biofilms. *Front. Cell. Infect. Microbiol.* **5**, 10 (2015).
7. Akram, W. et al. Hydroxyapatite coating for control degradation and parametric optimization of pure magnesium: an electrophoretic deposition technique for biodegradable implants. *J. Mater. Res. Technol.* **26**, 2587–2600 (2023).
8. Mohammadi, H. et al. Advances in silicon nitride ceramic biomaterials for dental applications—A review. *J. Mater. Res. Technol.* **28**, 2778–2791. <https://doi.org/10.1016/j.jmrt.2023.12.186> (2024).
9. O'Hagan-Wong, K., Enax, J., Meyer, F. & Ganss, B. The use of hydroxyapatite toothpaste to prevent dental caries. *Odontology* **110**, 223–230. <https://doi.org/10.1007/s10266-021-00675-4> (2022).
10. Gopi, D., Ramya, S., Rajeswari, D., Karthikeyan, P. & Kavitha, L. Strontium, cerium co-substituted hydroxyapatite nanoparticles: Synthesis, characterization, antibacterial activity towards prokaryotic strains and in vitro studies. *Colloids Surf., A* **451**, 172–180. <https://doi.org/10.1016/j.colsurfa.2014.03.035> (2014).
11. Riaz, M. et al. Synthesis of monophasic ag doped hydroxyapatite and evaluation of antibacterial activity. *Mater. Sci. Engineering: C* **90**, 308–313. <https://doi.org/10.1016/j.msec.2018.04.076> (2018).
12. AlSalem, H. S. et al. Physico-chemical and biological responses for hydroxyapatite/ZnO/graphene oxide nanocomposite for biomedical utilization. *Mater. Chem. Phys.* **283**, 125988. <https://doi.org/10.1016/j.matchemphys.2022.125988> (2022).
13. Özkaya, S. & Güler, O. in *Studies in Natural Products Chemistry* 82 (ed Rahman Atta ur) 55–112 (Elsevier, 2024).
14. Akhavan, A., Sheikh, N., Khoylou, F., Naimian, F. & Ataeivarjovi, E. Synthesis of antimicrobial silver/hydroxyapatite nanocomposite by gamma irradiation. *Radiat. Phys. Chem.* **98**, 46–50 (2014).

15. Karimzadeh, A., Koloor, S., Petrù, M., Ayatollahi, M. & Yahya, M. Damage characterization of dental nanocomposite adhesive in orthodontic treatment applications. *Int. J. Damage Mech.* **31**, 1299–1319 (2022).
16. Karimzadeh, A., Koloor, R., Ayatollahi, S., Bushroa, M. R., Yahya, M. Y. & A. R. & Assessment of nano-indentation method in mechanical characterization of heterogeneous nanocomposite materials using experimental and computational approaches. *Sci. Rep.* **9**, 15763 (2019).
17. Albalwi, H. A. et al. Medical applications of ternary nanocomposites based on hydroxyapatite/ytterbium oxide/graphene oxide: potential bone tissue engineering and antibacterial properties. *J. Mater. Res. Technol.* **18**, 4834–4845 (2022).
18. El-Naggar, M. E. et al. Tailoring combinations of hydroxyapatite/cadmium selenite/graphene oxide based on their structure, morphology, and antibacterial activity. *J. Inorg. Organomet. Polym Mater.* **32**, 311–325. <https://doi.org/10.1007/s10904-021-02115-w> (2022).
19. Almotiri, R. A. & Alkhamisi, M. M. Physico-chemical behavior and microstructural manipulation of nanocomposites containing hydroxyapatite, alumina, and graphene oxide. *Appl. Phys. A.* **128**, 351. <https://doi.org/10.1007/s00339-022-05479-z> (2022).
20. El-Morsy, M. A., Awwad, N. S., Ibrahim, H. A. & Menazea, A. A. Tuning the composition of Hydroxyapatite/Holmium oxide/Graphene oxide mixed systems for biomedical applications. *J. Inorg. Organomet. Polym Mater.* **33**, 76–89. <https://doi.org/10.1007/s10904-022-02436-4> (2023).
21. Afifi, M. et al. Improvement of physicochemical properties of ternary nanocomposites based on hydroxyapatite/CuO/graphene oxide for biomedical usages. *Ceram. Int.* **48**, 3993–4004. <https://doi.org/10.1016/j.ceramint.2021.10.186> (2022).
22. Eldrehmy, E. H. et al. Hydroxyapatite-based bio-ceramic of ternary nanocomposites containing cuprous oxide/graphene oxide for biomedical applications. *Diam. Relat. Mater.* **126**, 109121. <https://doi.org/10.1016/j.diamond.2022.109121> (2022).
23. Ghosh, R., Das, S., Mallick, S. P. & Beyene, Z. A review on the antimicrobial and antibiofilm activity of doped hydroxyapatite and its composites for biomedical applications. *Mater. Today Commun.* **31**, 103311. <https://doi.org/10.1016/j.mtcomm.2022.103311> (2022).
24. George, S. M., Nayak, C., Singh, I. & Balani, K. Multifunctional hydroxyapatite composites for orthopedic applications: A review. *ACS Biomaterials Sci. Eng.* **8**, 3162–3186. <https://doi.org/10.1021/acsbiomaterials.2c00140> (2022).
25. Jan, T. et al. Synthesis, physical properties and antibacterial activity of metal oxides nanostructures. *Mater. Sci. Semiconduct. Process.* **21**, 154–160. <https://doi.org/10.1016/j.mssp.2014.01.006> (2014).
26. Brayner, R. et al. Toxicological impact studies based on Escherichia coli bacteria in ultrafine ZnO nanoparticles colloidal medium. *Nano Lett.* **6**, 866–870 (2006).
27. Rana, A. et al. Tailoring dual S-Scheme based g-C3N4/ZnO/TiO2 ternary photocatalytic system immobilized on floating Cork for environmental remediation. *J. Taiwan Inst. Chem. Eng.* **168**, 105914. <https://doi.org/10.1016/j.jtice.2024.105914> (2025).
28. Soni, V. et al. Fabricating cattle dung-derived nitrogen-doped Biochar supported oxygen-deficient ZnO and Cu2O-based novel step-scheme photocatalytic system for aqueous Doxycycline hydrochloride mitigation and cr (VI) reduction. *J. Environ. Chem. Eng.* **11**, 110856. <https://doi.org/10.1016/j.jece.2023.110856> (2023).
29. Batra, V., Kaur, I., Pathania, D., Chaudhary, V. & Sonu & Efficient dye degradation strategies using green synthesized ZnO-based nanoplatforms: A review. *Appl. Surf. Sci. Adv.* **11**, 100314. <https://doi.org/10.1016/j.apsadv.2022.100314> (2022).
30. Hashim, N. C., Frankel, D. & Nordin, D. Graphene oxide-modified hydroxyapatite nanocomposites in biomedical applications: a review. *Ceramics-Silikaty* (2019).
31. Li, M. et al. An overview of graphene-based hydroxyapatite composites for orthopedic applications. *Bioactive Mater.* **3**, 1–18. <https://doi.org/10.1016/j.bioactmat.2018.01.001> (2018).
32. Roy, R. K. *Design of Experiments Using the Taguchi Approach: 16 Steps To Product and Process Improvement* (Wiley, 2001).
33. Adam, R. E., Pozina, G., Willander, M. & Nur, O. Synthesis of ZnO nanoparticles by co-precipitation method for solar driven photodegradation of congo red dye at different pH. *Photonics Nanostructures-Fundamentals Appl.* **32**, 11–18 (2018).
34. Imani, M. M., Kiani, M., Rezaei, F., Souri, R. & Safaei, M. Optimized synthesis of novel hydroxyapatite/CuO/TiO2 nanocomposite with high antibacterial activity against oral pathogen Streptococcus mutans. *Ceram. Int.* **47**, 33398–33404. <https://doi.org/10.1016/j.ceramint.2021.08.246> (2021).
35. Chahardoli, A. et al. Optimum green synthesis of silver nanoparticles with the highest antibacterial activity against streptococcus mutans biofilm. *Journal of Nanomaterials* 6261006 (2022). (2022).
36. Safaei, M. & Moghadam, A. Optimization of the synthesis of novel alginate-manganese oxide Bionanocomposite by Taguchi design as antimicrobial dental impression material. *Mater. Today Commun.* **31**, 103698. <https://doi.org/10.1016/j.mtcomm.2022.103698> (2022).
37. Abraham, J., Jose, B., Jose, A. & Thomas, S. Characterization of green nanoparticles from plants. in *Phytonanotechnology*. (eds N. Thajuddin Silvy Mathew) 21–39 (Elsevier, 2020).
38. Diputra, A. H., Dinatha, H., Yusuf, Y. & I. K. & A comparative X-ray diffraction analysis of Sr2+ substituted hydroxyapatite from sand Lobster shell waste using various methods. *Helijon* **11**, e41781. <https://doi.org/10.1016/j.helijon.2025.e41781> (2025).
39. Monshi, A., Foroughi, M. R. & Monshi, M. R. Modified scherrer equation to estimate more accurately nano-crystallite size using XRD. *World J. Nano Sci. Eng.* **2**, 154–160. <https://doi.org/10.4236/wjnse.2012.23020> (2012).
40. Go, A. D., Rosa, Camacho, F. M., Punzalan, E. R. & D. H. & Dataset on photocatalytic degradation of Levofloxacin using hydroxyapatite photocatalyst: optimization by response surface methodology. *Data Brief.* **42**, 108219. <https://doi.org/10.1016/j.dib.2022.108219> (2022).
41. Mirjallili, F., Mohammadi, H., Azimi, M., Hafezi, M. & Abu Osman, N. A. Synthesis and characterization of β -TCP/CNT nanocomposite: Morphology, microstructure and in vitro bioactivity. *Ceram. Int.* **43**, 7573–7580. <https://doi.org/10.1016/j.ceramint.2017.03.049> (2017).
42. Gezaz, M. S., Aref, S. M. & Khatamian, M. Investigation of structural properties of hydroxyapatite/zinc oxide nanocomposites; an alternative candidate for replacement in recovery of bones in load-tolerating areas. *Mater. Chem. Phys.* **226**, 169–176 (2019).
43. Zhu, J., Fan, C., Ning, C. & Wang, W. Cathodic electrophoretic deposited HA-rGO-ZnO ternary composite coatings on ZK60 magnesium alloy for enhanced corrosion stability. *Ceram. Int.* **49**, 37604–37622. <https://doi.org/10.1016/j.ceramint.2023.09.087> (2023).
44. Wu, J. et al. Preparation and properties of GO/ZnO/nHAp composite microsphere bone regeneration material. *Micromachines* **15**, 122. <https://doi.org/10.3390/mi15010122> (2024).
45. Bouras, M., Boumaiza, A., Ji, V. & Rouag, N. XRD peak broadening characterization of deformed microstructures and heterogeneous behavior of carbon steel. *Theoret. Appl. Fract. Mech.* **61**, 51–56 (2012).
46. Devi, P. G. & Velu, A. S. Synthesis, structural and optical properties of pure ZnO and Co doped ZnO nanoparticles prepared by the co-precipitation method. *J. Theoretical Appl. Phys.* **10**, 233–240. <https://doi.org/10.1007/s40094-016-0221-0> (2016).
47. Subasi, B. S. et al. Photocatalytic degradation of Tetracycline from aqueous solution with graphene oxide and hydroxyapatite composites. *Sci. Rep.* **15**, 25894 (2025).
48. Sumathra, M., Sadasivuni, K. K., Kumar, S. S. & Rajan, M. Cisplatin-loaded graphene oxide/chitosan/hydroxyapatite composite as a promising tool for osteosarcoma-affected bone regeneration. *Acs Omega* **3**, 14620–14633 (2018).
49. Heshmatpour, F. & Haghbin, S. Nanohydroxyapatite/graphene oxide nanocomposites modified with synthetic polymers: promising materials for bone tissue engineering applications. *Int. J. Polym. Mater. Polym. Biomaterials.* **70**, 585–591 (2021).
50. Sirajunisha, H., Sakthivel, P. & Balakrishnan, T. Structural, photoluminescence, antibacterial and biocompatibility features of zinc incorporated hydroxyapatite nanocomposites. *J. Mater. Sci.: Mater. Electron.* **32**, 5050–5064. <https://doi.org/10.1007/s10854-021-5239-4> (2021).

51. Rulis, P., Ouyang, L. & Ching, W. Electronic structure and bonding in calcium apatite crystals: Hydroxyapatite, fluorapatite, chlorapatite, and bromapatite. *Phys. Rev. B—Condensed Matter Mater. Phys.* **70**, 155104. <https://doi.org/10.1103/PhysRevB.70.155104> (2004).
52. Alam, S. N., Sharma, N. & Kumar, L. Synthesis of graphene oxide (GO) by modified hummers method and its thermal reduction to obtain reduced graphene oxide (rGO). *Graphene* **6**, 1–18 (2017).
53. Boyapati, P.C.S., Srinivas, K. & Chandu, B. Green synthesis of graphene-hydroxyapatite nanocomposites with improved mechanical properties for bone implant materials. *Mater. Chem. Phys.* **296**, 127331. <https://doi.org/10.1016/j.matchemphys.2023.127331> (2023).
54. Singh, J., Kaur, S., Kaur, G., Basu, S. & Rawat, M. Biogenic ZnO nanoparticles: A study of blueshift of optical band gap and photocatalytic degradation of reactive yellow 186 dye under direct sunlight. *Green. Process. Synthesis.* **8**, 272–280. <https://doi.org/10.1515/gps-2018-0084> (2019).
55. Arularasu, M. V. Biosynthesis, structural characterization and humidity sensing properties of cellulose/ZnO nanocomposite. *Sens. Bio-Sensing Res.* **45**, 100673. <https://doi.org/10.1016/j.sbsr.2024.100673> (2024).
56. Kobylukh, A. et al. Effect of graphene material structure and iron oxides deposition method on morphology and properties of graphene/iron oxide hybrids. *Appl. Surf. Sci.* **573**, 151567. <https://doi.org/10.1016/j.apsusc.2021.151567> (2022).
57. Wu, J., Zheng, X., Lv, Y., Li, Y. & Zhang, G. Preparation and characterization of GO/ZnO/Ag nanocomposites and their synergistic antibacterial effect on Streptococcus mutans. *AIP Adv.* **13** <https://doi.org/10.1063/5.0137874> (2023).
58. Zhou, S. & Bongiorno, A. Origin of the chemical and kinetic stability of graphene oxide. *Sci. Rep.* **3**, 2484. <https://doi.org/10.1038/srep02484> (2013).
59. Cengiz, B., Gokce, Y., Yildiz, N., Aktas, Z. & Calimli, A. Synthesis and characterization of hydroxyapatite nanoparticles. *Colloids Surf. A* **322**, 29–33. <https://doi.org/10.1016/j.colsurfa.2008.02.011> (2008).
60. Wan, B. et al. Biomimetically precipitated nanocrystalline hydroxyapatite. *Nano TransMed.* **1**, e9130008. <https://doi.org/10.26599/NTM.2022.9130008> (2022).
61. Ahmed, M., Afifi, M., Ashraf, S., Abdelbadie, S. A. & Baltrusaitis, J. Efficient antibacterial activity of ternary nanocomposites containing hydroxyapatite, Co₃O₄, and cerium oxide. *Mater. Chem. Phys.* **305**, 127856. <https://doi.org/10.1016/j.matchemphys.2023.127856> (2023).
62. Singh, S., Singh, G. & Bala, N. Synthesis and characterization of iron oxide-hydroxyapatite-chitosan composite coating and its biological assessment for biomedical applications. *Prog. Org. Coat.* **150**, 106011. <https://doi.org/10.1016/j.porgcoat.2020.106011> (2021).
63. Younis, A. B., Haddad, Y., Kosaristanova, L. & Smerkova, K. Titanium dioxide nanoparticles: recent progress in antimicrobial applications. *WIREs Nanomed. Nanobiotechnol.* **15**, e1860. <https://doi.org/10.1002/wnan.1860> (2023).
64. Safaei, M. et al. Application of Taguchi method in the optimization of synthesis of cellulose-MgO Bionanocomposite as antibacterial agent. *Pol. J. Chem. Technol.* **21**, 116–122. <https://doi.org/10.2478/pjct-2019-0047> (2019).
65. Roy, R. K. *A Primer on the Taguchi Method, Second Edition* (Society of Manufacturing Engineers, 2010).
66. Liu, S. et al. Antibacterial activity of graphite, graphite oxide, graphene oxide, and reduced graphene oxide: membrane and oxidative stress. *ACS Nano.* **5**, 6971–6980. <https://doi.org/10.1021/nn202451x> (2011).
67. Acharya, G. et al. CHK1 inhibitor induced parylation by targeting PARG causes excessive replication and metabolic stress and overcomes chemoresistance in ovarian cancer. *Cell. Death Discov.* **10**, 278. <https://doi.org/10.1038/s41420-024-02040-0> (2024).
68. Okechukwu, C. C. et al. Enhanced therapeutic efficacy of the nanoscale fluoropyrimidine polymer CF10 in a rat colorectal cancer liver metastasis model. *Cancers (Basel).* **16**, <https://doi.org/10.3390/cancers16071360> (2024).

Author contributions

Conceptualization, investigation, data curation, and writing—original draft were performed by H.M., and N.B.; validation, visualization, methodology, formal analysis, and revision/review/editing—original draft were performed by H.M., N.B., M.P., S.B., M.E., M.S., and S.S.R.K.; supervision, project administrations, resources, and funding acquisition were performed by M.P., S.B., M.S., and S.S.R.K. All authors have read and agreed to the published version of the manuscript.

Funding

Open Access funding provided by Czechelib agreement with Springer Nature.

Declarations

Competing interests

The authors declare no competing interests.

Additional information

Correspondence and requests for materials should be addressed to M.S. or S.S.R.K.

Reprints and permissions information is available at www.nature.com/reprints.

Publisher's note Springer Nature remains neutral with regard to jurisdictional claims in published maps and institutional affiliations.

Open Access This article is licensed under a Creative Commons Attribution-NonCommercial-NoDerivatives 4.0 International License, which permits any non-commercial use, sharing, distribution and reproduction in any medium or format, as long as you give appropriate credit to the original author(s) and the source, provide a link to the Creative Commons licence, and indicate if you modified the licensed material. You do not have permission under this licence to share adapted material derived from this article or parts of it. The images or other third party material in this article are included in the article's Creative Commons licence, unless indicated otherwise in a credit line to the material. If material is not included in the article's Creative Commons licence and your intended use is not permitted by statutory regulation or exceeds the permitted use, you will need to obtain permission directly from the copyright holder. To view a copy of this licence, visit <http://creativecommons.org/licenses/by-nc-nd/4.0/>.